PCCP

Accepted Manuscript

ROYAL SOCIETY OF CHEMISTRY

www.rsc.org/pccp

A Combined Computational and Experimental Investigation of Mg Doped α-Fe_2O_3

Monica Kosa,[†] Hannah Noa Barad,[†] Vijay Singh, David A. Keller, Klimentiy Shimanovich, Sven Rühle, Assaf Y. Anderson, Arie Zaban, Dan Thomas Major*

Department of Chemistry and the Lise Meitner-Minerva Center of Computational Quantum Chemistry and the Institute for Nanotechnology and Advanced Materials, Bar-Ilan University, Ramat-Gan 52900, Israel

KEYWORDS: α-Fe_2O_3, all oxide photovoltaics, transition metal oxides, DFT, bandgap

Abstract

In the current work, pristine α-Fe_2O_3 metal oxide was doped with Mg in an attempt to modulate its electronic properties. To this end, we employed an experimental high throughput strategy, including scanning XRD and optical spectroscopy, which were complimented by atomistic density functional theory (DFT) calculations. The combined study reveals that at Mg/Fe atomic ratios up to ~1/3, the bandgaps of the hematite-Mg composite materials are similar to that of the pure material. The observed bandgaps are rationalized by electronic band structure and density of states calculations. Additional rational for the similar bandgaps in pure and doped hematite is provided by topological Bader charge analyses, which indicate that the Mg and Fe ions in the hematite matrix have similar partial atomic charges. Nonetheless, the small charge density difference between the Mg and Fe ions induces a slight spin polarization on both oxygen and Fe ions, resulting in changes in the band edges. Further charge density analyses, using charge density maps and chemical-bonding analyses with the crystal orbital Hamiltonian population scheme, indicate that Mg forms ionic bonds with the neighboring oxygen atoms. This change from iron-oxygen covalent bonds to a more ionic nature for magnesium-oxygen bonds is probably responsible for the reduction observed in the computed bulk modulus of α-$Mg_{0.17}Fe_{1.83}O_3$ (193 GPa) compared to α-Fe_2O_3 (202 GPa).

Introduction

Hematite (α-Fe_2O_3) is an attractive metal oxide for potential use in solar water splitting,[1-4] as well as for photovoltaics,[5] due to its chemical stability, abundance and non-toxicity. Fe_2O_3/MgO composites have been tested for various catalytic energy materials applications such as H_2O_2 decomposition catalysis[6] and enhanced arsenic adsorption performance.[7] Hematite can be manufactured by several methods, including atomic layer deposition (ALD), pulsed laser deposition (PLD) or spray pyrolysis. In spite of its many favorable properties, hematite is not a practical material for photovoltaic applications due to poor charge transport, which is a result of limited small-polaron mobility (i.e. the electron hopping between adjacent sites, which is accompanied by geometrical changes within proximal lattice sites[8]), and a bandgap of ca. 2.1 eV, which is not optimal for the solar spectrum. This implies that many physical features, such as bandgap and structural and mechanical properties,[9] must be improved in order to make this material attractive for photonic water splitting and photovoltaic applications.

In order to modulate the photon absorbing abilities of potential photovoltaic materials, bandgap engineering has emerged as a promising direction and has drawn attention from both the experimental and computational scientific communities.[10, 11] Such engineering can be achieved by replacing individual atoms in the hematite structure by different metal and non-metal atoms, i.e. both Fe and O in pure hematite can be considered for substitution.

The crystal structure of hematite has layers of oxygen atom separated by layers of iron atoms. The iron ion is in a formal +3 oxidation state, and has a half-filled band (i.e. $3d^5$configuration). The magnetic ordering within each Fe-layer is ferromagnetic and in-between layers the ordering is antiferromagnetic.[12] In order to optimize the photoactivity of hematite, the band structure of pure and 3*d* transition metal incorporated hematite was investigated computationally by several research groups using density functional theory (DFT). Huda et al. studied Sc, Ti, Cr, Mn and Ni incorporated hematite at the local spin density approximation level with on-site Hubbard correction (LSDA+U level of theory) and found that the crystal cell parameters increase for the Sc and decrease for Ti, Cr, Mn and Ni incorporated hematite.[13] These transition metals also have a marked effect on the density of states (DOS) of doped hematite. The band due to Sc mixes well with the original conduction band of hematite, while Ni produces two additional states in the center of the gap. The observed trend was rationalized by an increased localization of the *d* orbitals as one moves across the periodic table from Sc to Ni.[13] Yang et al. studied transition metal doped hematite at the LSDA+U level of theory as well.[14] Interestingly, the authors noted that for Cu and Cd half-substituted hematite, the bandgap does not change significantly for the spin up channel. However, for the down spin channel, they observed a band crossing of the Fermi level, indicating half-metallic behavior.[14] Recently, Xia et al. attempted substitution of the oxygen atom by sulfur at the DFT generalized

gradient approximation (GGA) level of theory with Hubbard correction (GGA+U). Their study revealed that at an S concentration of 5.6%, a direct band gap of 1.45 eV is obtained.[15] Pozun et al. studied bandgap properties of doped hematite using hybrid DFT. In this work, all transition metal and *p*-block elements were examined as substituent atoms for a single Fe atom in a 120 atom supercell, and it was found that the HOMO-LUMO gap changes are due to the addition of states into the bandgap region.[10]

Several experimental works also tackled the properties of a variety of doped hematite analogues. Experimentally it was found that the bandgap of nanoporous hematite produced by spray pyrolysis substantially decreases upon Ti doping.[16] Si doped hematite, deposited by spin coating followed by heat treatment,[17] as well as Ti and Sn co-doped anodic deposited hematite, showed only minor changes of the bandgap.[18] Mohanty et al. measured an indirect bandgap for both pure hematite and Mg doped hematite, of 2.135 eV and ~2.5 eV, respectively.[19] Recently, Tang et al. interpreted the Tauc plots as suggesting an increase in the bandgap with increasing Mg concentrations. In that study, the reported atomic Mg concentration was as high as 8.1% under Ar/O_2 atmosphere.[20]

In the present study, we introduce thin films of Mg doped hematite as an alternative to transition metal doping, in an attempt to modify the bandgap of α-Fe_2O_3. Reduction of the α-Fe_2O_3 bandgap can make this material more viable as a photovoltaic device, as well as a catalyst for water splitting. We present optical bandgaps measured on a thin film of Mg-doped hematite with different Mg/Fe atomic ratios, obtained using continuous compositional spreads (CCS) produced by PLD. These thin-film properties are compared to atomistic DFT calculations.

Methods

I. Experimental methods

Combinatorial material libraries with a CCS were used to investigate the properties of hematite as a function of the concentration of Mg substituent. The libraries were produced on alkaline free glass with a size of 71 x 71 mm^2. The libraries were deposited by pulsed laser deposition using a commercial system (Neocera) consisting of a KrF excimer laser with an emission wavelength at 248 nm (Coherent Compex-Pro102). The pulsed laser energy was ~1.8 J/cm^2, and was focused onto the target to a 0.07 mm^2 spot area, at a repetition rate of 8 Hz. The target to sample distance was 52 mm, and the deposition was carried out at an oxygen pressure of 7 mTorr, while the substrate heater was adjusted to 500 ˚C.

A pure hematite library was deposited using 30,000 laser pulses. To produce a CCS library, 60 pulses from a Fe_2O_3 target (99% pure, Kurt J. Lesker Co.) were deposited with the center of the plasma plume close to one edge of the glass. The glass substrate was rotated by 180º and the Fe_2O_3 target was switched with an MgO target (99% pure, Kurt J. Lesker Co.), from which 2 pulses were deposited, Figure

1. The rotation cycle was repeated 500 times to produce a library with a maximum film thickness of 400 nm at the peak deposition of the Fe_2O_3. The small number of pulses during each cycle guaranteed deposition with a thickness on the order of the crystal unit cell. The unit-cell-per-pulse deposition in conjunction with substrate heating, achieved optimal intermixing of the two materials throughout the library.

Separate depositions of Fe_2O_3 and MgO at room temperature, with a sticker glued to the substrate that had a grid of holes as a shadow mask, were used to measure the thickness profile of the two materials using a scanning profilometer (Dektak 150). The doping density was calculated based on the thickness profiles of the pure materials, which are superimposed in a CCS library.

Thin film X-ray diffraction measurements (XRD) with mapping capabilities (Rigaku SMARTLAB) were used to evaluate the crystal structure of the pure hematite and CCS libraries. The θ-2θ (40 kV, CuKα) scans were performed in a range from 25˚ to 80˚, at a scan rate of 1˚/min. Optical measurements were carried out using an automated scanning system in combination with an optical fiber based system consisting of two integrating spheres and a CCD array of spectrometers (USB4000, Ocean Optics). The total reflectance, total transmission, and specular reflection were measured on an array of 13 x 13 points in the library.[21] The bandgap was subsequently derived from Tauc plots. The error in the optical measurements is 0.1%.

II. Computational methods

The calculations were performed with the VASP 5.2.12 program,[22-25] using the projector augmented wave (PAW)[26, 27] pseudo potentials (PP) method, see Supporting Information for additional details. Plane wave energy cutoffs of 500 and 700 eV were tested in conjunction with the PBE[28] functional. The energy cutoffs of 500 and 700 eV produced nearly identical geometrical, electronic density of states (DOS) and Bader analysis results (Supporting Information, Table S1a, S1b and Fig. S1). The PBE functional was augmented with a Hubbard on-site potential, with U=4.3 eV[29] for the *d* states of Fe, within the GGA+U approach.[30] A gamma point centered grid was used with a *k*-point distance of 0.2. The cell parameters and geometries of all structures were optimized until the forces converged to <0.002 eV/Å.

Bader charge analysis was performed on the all-electron densities (the core density was generated from the PP files).[31-34] Based on the experimental XRD analysis, which indicated that the hematite crystal structure is preserved upon incorporation of Mg, the computational model assumed substitutional Mg doping.

To study the effect of incorporating Mg, a single Fe atom was replaced by an Mg atom in hexagonal unit cells of 30 (1x1x1), 60 (1x2x1), and 120 (2x2x1) atoms, thus mimicking different Mg concentrations. The Mg/Fe ratios correspond to 1/11, 1/23, 1/47 and the corresponding chemical compositions are $Mg_{0.17}Fe_{1.83}O_3$, $Mg_{0.08}Fe_{1.92}O_3$, and $Mg_{0.04}Fe_{1.96}O_3$. For the ratio 1/11, in addition to the 30 atoms simula-

tion cell, we also computed the 60 atoms configuration cell, which contains 2 Mg atoms, 22 Fe atoms and 36 O atoms. 7 different arrangements of the 2 Mg atoms within the unit cell were evaluated. The lowest energy configuration corresponds to the atomic arrangement in which the 2 Mg atoms occupy the same layer (see conf. a in Table S2). We note that such an arrangement induces spin polarization in the simulation cell. This configuration is lower in energy than conf. f (see Table S2), for example, in which the two Mg atoms occupy different layers, resulting in zero net spin of the simulation cell. The results obtained with the 60 atoms cell mirror those obtained for the 30 atoms cell.

An antiferromagnetic interlayer ordering was assumed, as it is the lowest energy magnetic configuration of hematite.[12] For studying the band structure of pure and Mg alloyed hematite a set of special *k*-points was generated using the *ACONVASP-online* facility, (Fig. S2).[35]

The electronic structure study of α-Fe_2O_3 and $Mg_{0.17}Fe_{1.83}O_3$, was further complemented by computing the optical properties of Fe_2O_3 and $Mg@Fe_2O_3$, in the PAW framework using the method of Gajdoš et al.[36] In this approach, we compute the imaginary part of the macroscopic dielectric tensor, which is directly related to the optical absorption spectrum of any material.[37-39]

To evaluate the nature of the chemical bonds, we plotted the crystal orbital Hamiltonian population (COHP)[40-42] for the spin densities of α-Fe_2O_3 and $Mg_{0.17}Fe_{1.83}O_3$, focusing on the Fe-O and Mg-O nearest neighbor bonds. We employed the LOBSTER program, which calculates COHPs directly from the plane-waves.[42] COHP provides the energy resolved visualization of chemical bonding in solids based on DFT calculations, by rewriting the band structure energy as a sum of energy per orbital contribution. An energy integral of COHP (ICOHP) provides access to the contribution of an atom or a chemical bond to the distribution of the one particle energy. The validity of the method has previously been shown by application to chemical textbook examples like diamond, GaAs, CsCl, and Na and several different classes of solid-state materials.[40-43]

To evaluate the bulk moduli, B, of α-Fe_2O_3 and $Mg_{0.17}Fe_{1.83}O_3$, we optimized the volume and shape of the cell subjugated to several values of pressure, using the PSTRESS keyword in VASP. For these calculations, the plane-wave energy cutoff was increased to 750 eV, and the keyword ADDGRID=.TRUE. was used to add a support-grid for the evaluation of the augmentation charges, as this reduces the numerical noise in the computed forces.

Results and Discussion

I. Experimental Results

i. Structure of pure and Mg alloyed Fe_2O_3.

The Fe_2O_3-MgO library is deposited as a continuous compositional spread (CCS) on an alkaline-free glass substrate. To obtain the CCS layer, a small amount of each material is ablated per deposition cycle, thus good intermixing between materials is achieved. A schematic presentation of the Fe_2O_3-MgO CCS library is presented in Fig. 1.

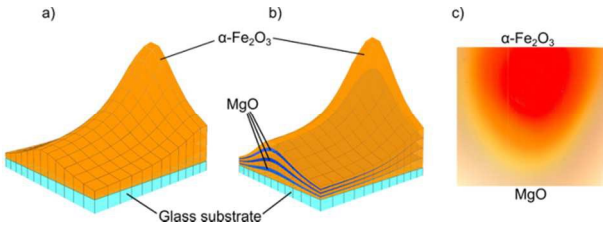

Figure 1. Schematic representation of the a) pure hematite library, and b) the CCS Fe_2O_3-MgO library. The light-blue bottom depicts the glass substrate, while the orange is the α-Fe_2O_3 deposition, and the dark blue is the MgO deposition. Each layer of α-Fe_2O_3 and MgO is one deposition cycle. Deposition of the layers was repeated 500 times. c) An actual image of the deposited CCS library, where the top part (red-orange) is the α-Fe_2O_3 maximum thickness and the other edge (180˚) is the MgO maximum thickness, which is transparent in visible light.

The ratio between the Fe and Mg atoms is calculated based on the thickness profiles, which are measured for each of the materials separately and based on their theoretical densities, as shown in Fig. 2. The Mg/Fe atomic ratio is between 0-1 for areas of the library that have more Fe_2O_3, which is most of the library. The areas in the library that have an Mg/Fe atomic ratio of 1 or higher are the areas where the MgO deposition is thickest. In this case the Mg atoms either completely replace the Fe in Fe_2O_3, or form a separate MgO phase.

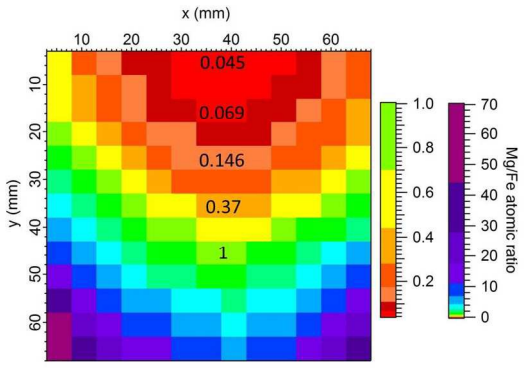

Figure 2. Fe to Mg atomic ratios, calculated based on the α-Fe_2O_3 and MgO thickness profiles and densities. The right scale bar includes the ratios over the entire library, and the left scale bar is enlarged for the Mg/Fe ratios from 0 to 1.

XRD measurements were used to map the Fe_2O_3-MgO library (Fig. 3). XRD mapping of a library deposited using only a Fe_2O_3 target displays peaks that belong to pure α-Fe_2O_3, (Fig. S3). In contrast, mapping of the Fe_2O_3-MgO CCS library shows some peaks that differ from the pure hematite phase. For an Mg/Fe atomic ratio of 0.045, the XRD spectrum contains the peaks for the hematite phase, and also a new peak, indicating that an unidentified Mg-Fe_2O_3 phase is formed. For an Mg/Fe atomic ratio of 0.069 and 0.146 the peak intensity of the unidentified Mg-Fe_2O_3 phase increases.

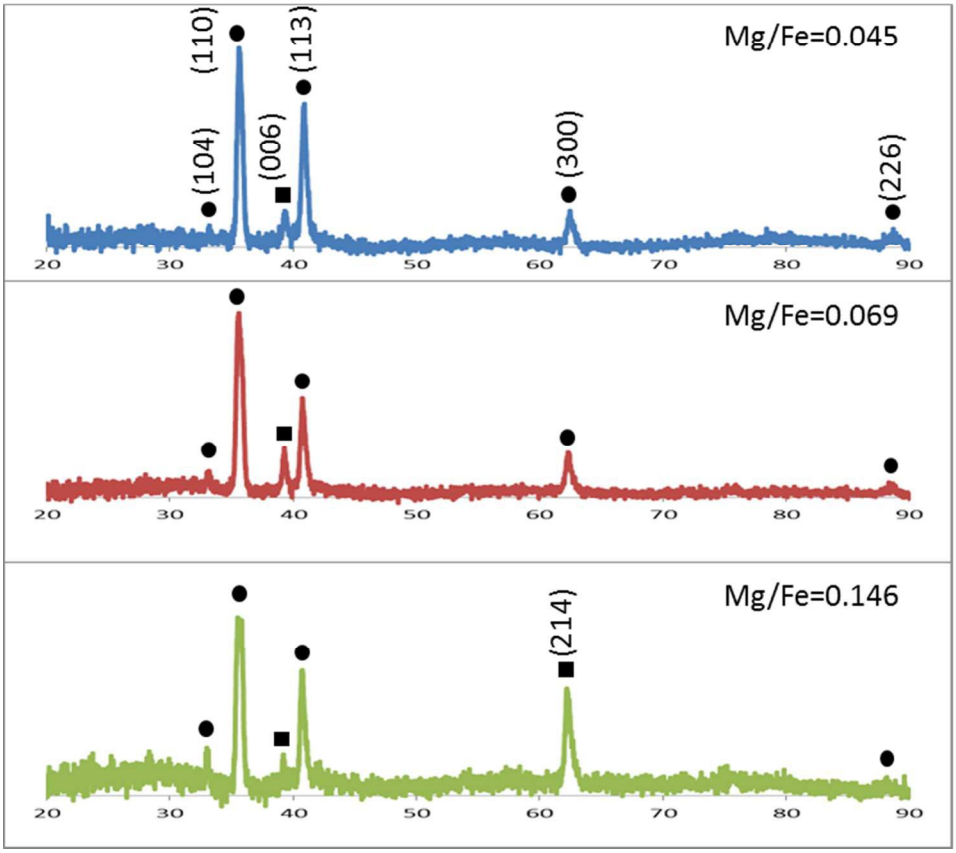

Figure 3. X-ray diffraction spectra of Mg doped hematite, Mg/Fe atomic ratios of 0.045 (blue), 0.069 (red) and 0.146 (green). Circles represent the peaks corresponding to the α-Fe_2O_3 phase, and the squares represent the peaks corresponding to the Mg-Fe_2O_3 mixed phase.

ii. Optical bandgap.

Optical measurements, including total transmission (TT) and total reflection (TR), were carried out on the Fe_2O_3-MgO CCS library. The absorbance (Abs) for every point in the library is derived as:

(eq. 1) Abs= 1-TT-TR

The absorbance (Abs) is then used to calculate the absorption coefficient (α) for every Mg/Fe atomic ratio in the library by:

(eq. 2) $\alpha=(-\ln(1-Abs))/d$

where d is the total thickness of the Fe_2O_3-MgO CCS library. The bandgap is derived by plotting $(\alpha h\nu)^{1/2}$ as a function of the energy, hν (Tauc plot), taking into account that Fe_2O_3 has an indirect bandgap.[13] The linear regime in the Tauc plot is fitted using a linear fit function, and the bandgap is determined as the intercept point between the linear fit and the energy x-axis (Fig.4, Fig. S4, Fig. S5). The bandgaps found for the pure hematite library are 1.92-2.12 eV, in agreement with bandgaps reported in the literature.[19]

The bandgaps obtained for the Fe_2O_3-MgO CCS library are lower for some of the Mg/Fe atomic ratios, and range from 2.03 eV to 1.6 eV (full maps of the bandgaps can be found in Fig. S4). The higher bandgaps in the CCS library mostly belong to the pure Fe_2O_3 phase and the Mg-doped Fe_2O_3 phase.[44] A plot of the bandgap as a function of the Mg/Fe atomic ratio in the CCS library is given in Fig. 4. At low Mg/Fe atomic ratios up to 0.2 the bandgap remains within the range of the reported bandgap values.[19] For higher Mg/Fe atomic ratios (0.2 to 0.35), the bandgap is only slightly reduced to ~1.85, although the spread in the data increases. The spread in the data is probably due to the formation of both the pure and doped hematite and new Mg-Fe_2O_3 phases. The bandgap reduction likely arises from the new Mg-Fe_2O_3 phase or Mg doping of α-Fe_2O_3 (Fig. 3), in which Mg atoms may replace Fe atoms in hematite, thus changing the absorbance. The slight bandgap reduction can possibly make α-Fe_2O_3 more viable for photovoltaic applications or for water splitting, as the lower bandgap can collect photons from the IR region of the solar spectrum, and improve the absorber properties of α-Fe_2O_3. Experimentally, it can be concluded that small amounts of doping of Mg in hematite, up to ratios of Mg/Fe=0.2, do not significantly affect the absorption and bandgap of hematite. Furthermore, it seems that the hematite structure is maintained and that new Mg-Fe_2O_3 phases do not affect the structure of the hematite.

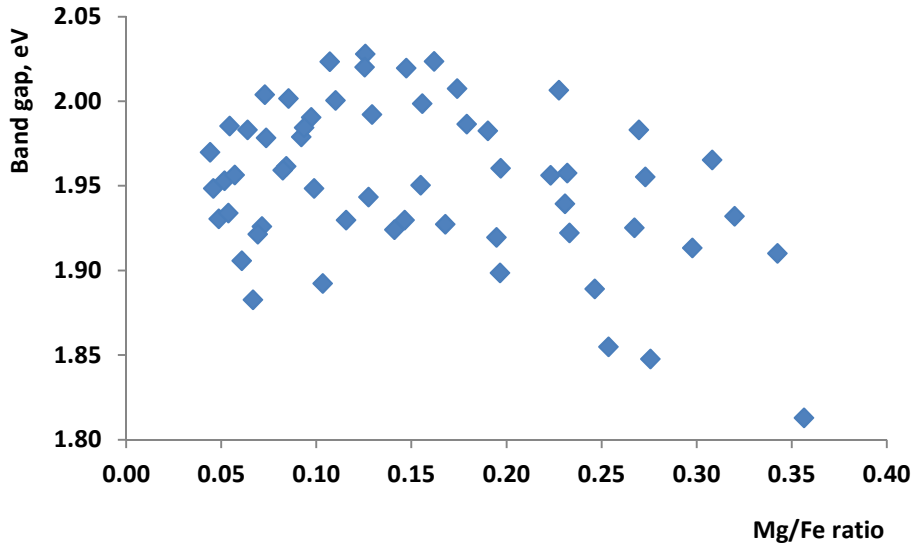

Figure 4. Bandgap vs. Mg/Fe atomic ratios, depicting a spread in the bandgap values for Mg/Fe atomic ratios up to ~0.35. The bandgap is derived by plotting $(\alpha h\nu)^{1/2}$ as a function of the energy, $h\nu$ (Tauc plot).

II. Computational Results

A. Structure

The cell parameters of pure and Mg doped hematite are shown in Table 1. For pure hematite, the volume of the monoclinic 30-atom unit cell is 313.56 $Å^3$. It remains practically unchanged, with a value of 313.75 $Å^3$, when one iron atom, is substituted with a magnesium atom. Structural parameters of larger monoclinic cells of pure hematite of 60 and 120 atoms also do not change with the inclusion of Mg atom, Table 1.

In the pristine hematite we obtain two sets of Fe-O bond lengths: three Fe-O bonds of 2.130 Å and three Fe-O bonds of 1.976 Å. In α-$Mg_xFe_{2-x}O_3$, x=0.17, the first set of Fe-O bonds slightly decreases to 2.096 Å and the second set increases to 1.989 Å. The Mg environment may be defined by two sets of Mg-O bonds as well, with values of 2.058 Å and 2.165 Å (each set has three Mg-O bonds). The minute change in Fe-O bond lengths upon incorporation of Mg, as well as the similarity between the Fe-O and Mg-O bond lengths, explains the almost unchanged global cell parameters. Similarly, for lower concentrations of Mg (x=0.08 and x=0.04), the cell parameters remain nearly identical to the pure system (Table 1, Table S3).

Table 1. Computed cell parameters for pure and Mg-alloyed hematite.

Cell Atom Composition	Expt.[45]	Pure α-Fe_2O_3		
		Atomic configuration of the simulation cell		
a, Å		12·Fe, 18·O	24·Fe, 36·O	48·Fe, 72·O
b, Å	5.038±0.002	5.097	5.097	10.193
c, Å		5.097	10.193	10.193
Volume of the unit cell, *V*, Å^3	13.772±0.012	13.937	13.938	13.938
		313.56	627.12	1254.18
		Mg-doped α-Fe_2O_3		
Cell Atom Composition		Atomic configuration of the simulation cell		
Mg/Fe atomic ratio		1·Mg, 11·Fe, 18·O	1·Mg, 23·Fe, 36·O	1·Mg, 47·Fe, 72·O
Chemical Formula		1/11=0.09	1/23=0.04	1/47=0.02
Cell Parameters		$Mg_{0.17}Fe_{1.83}O_3$	$Mg_{0.08}Fe_{1.92}O_3$	$Mg_{0.04}Fe_{1.96}O_3$
a, Å		5.096	5.094	10.194
b, Å		5.096	10.191	10.194
c, Å		13.949	13.938	13.937
Volume of the unit cell, V, Å^3		313.75	627.15	1254.20

B. Charge analysis

The average Bader charges and volumes for pure and doped hematite are shown in Table 2. The computed charge of the iron atom is 1.780 a.u. in the pure hematite. It remains practically unchanged (1.789 a.u.) for the highest concentration of Mg considered in this work, i.e. $Mg_{0.17}Fe_{1.83}O_3$. For lower concentrations of Mg, such as in $Mg_{0.04}Fe_{1.96}O_3$, we observe a small change, with a partial charge of 1.792 a.u. Interestingly, the computed Bader charges of magnesium incorporated into α-Fe_2O_3 is 1.719 a.u. This value remains very similar for all three concentrations considered in this work, and is very similar to the charge of 1.689 a.u. of Mg in pure MgO. This picture is consistent with the common notion that magnesium forms ionic compounds, with a constant charge of approximately +2 a.u. The negative charges of the oxygen atoms show small variations with varying Mg concentration, Table 2. Thus, introduction of Mg-ions into hematite induces only minor changes in the partial charges of iron and oxygen compared to pure hematite.

Table 2. Average computed Bader partial atomic charges (a.u.) and volumes (Å^3) of pure and Mg doped hematite and pure MgO rocksalt.

Computed cell composition			Atomic configuration of the simulation cell		
			1·Mg, 11·Fe, 18·O	1·Mg, 23·Fe, 36·O	1·Mg, 47·Fe, 72·O
Mg/Fe atomic ratio			1/11=0.09	1/23=0.04	1/47=0.02
	Pure α-Fe_2O_3	Pure MgO	$Mg_{0.17}Fe_{1.83}O_3$	$Mg_{0.08}Fe_{1.92}O_3$	$Mg_{0.04}Fe_{1.96}O_3$
Average Charges					
Mg	-	1.689	1.719	1.719	1.718
Fe	1.780	-	1.789	1.789	1.792
O	-1.186	-1.689	-1.189	-1.191	-1.193
Average Volumes					
Mg	-	4.813	4.938	4.924	4.891
Fe	8.305	-	8.202	8.216	8.195
O	11.883	14.457	12.138	12.035	12.002

The charge distribution in pure α-Fe_2O_3 and α-$Mg_{0.17}Fe_{1.83}O_3$ is shown in Fig. 5a and 5b. In pure α-Fe_2O_3, the charge is located in the Fe-O interatomic region (green arrow), indicating some covalent contribution to the iron-oxygen bond. In α-$Mg_{0.17}Fe_{1.83}O_3$, however, the Mg-O interatomic region does not have any electron density (at the presented density iso-value, green arrow), indicating a more ionic nature of the magnesium oxygen bond. This point will be discussed further below (Section D).

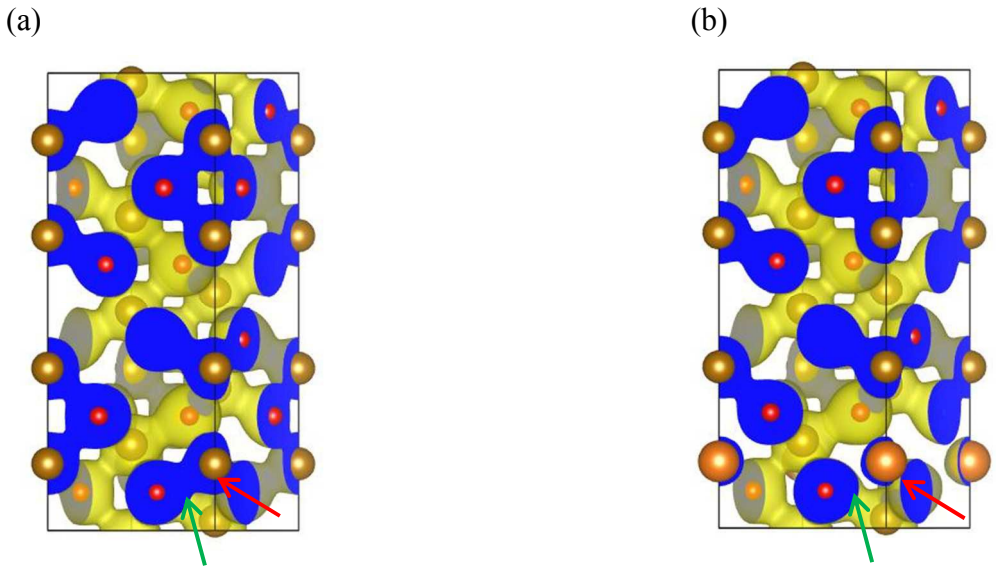

Figure 5. Charge distribution in (a) α-Fe_2O_3 and (b) $Mg_{0.17}Fe_{1.83}O_3$. The yellow color indicates the electron density located within the cell, at an iso-surface value of 0.05 el/Å^3. The blue color represents the electron density at the cell surface (which interacts with its periodic image). The red-brown spheres within the yellow electron density indicate the positions of the atoms (Fe, Mg, O). Red arrows indicate the (a) Fe and (b) Mg atoms at the substitution site. Green arrows point to the regions of cation-oxygen bonding.

C. Electronic density of states (DOS), band structure and optical absorption spectra.

The electronic DOS and band structure of pure and Mg alloyed hematite (α-$Mg_{0.17}Fe_{1.83}O_3$) are shown in Fig.6a,b and 7a-c. The Fermi level, E-Fermi, is set to 0.The DOS of pristine hematite, which has an antiferromagnetic spin ordering between the iron layers, shows that the spin up channel and the spin down channel are symmetric, with a bandgap of 2.01 eV. The top of the valence band is comprised of the oxygen 2*p* states, with a contribution from the iron 3*d* states. The bottom of the conduction band is comprised of mainly iron 3*d* states (see Fig. S6 for details). This picture is consistent with previous theoretical studies of hematite.[13]

With the introduction of Mg, the symmetry of the spin up and spin down channels is broken, with a concomitant polarization of both the O-2*p* and Fe-3*d* states. The gap in the spin up channel increases to 2.20 eV. Interestingly, in the spin down channel there is a band crossing of the E-Fermi. This is similar to the DOS structure of metals near the Fermi level (see Fig. S7 for details) and to previous computational studies on substitution doping of hematite.[14]

The band structure of pure and Mg doped hematite was computed for the high symmetry points of the hexagonal cell. The conduction band minimum (CBM) of α-Fe_2O_3 and α-$Mg_{0.17}Fe_{1.83}O_3$ remains similar with little dispersion. The valence band maximum (VBM) of the spin up channel is shifted slightly below its position with respect to E-Fermi in pure α-Fe_2O_3, while that of the spin down channel is shifted slightly up and thus crossing the E-Fermi at several points along the high symmetry lines of the hexagonal cell. Such a band structure of α-$Mg_{0.17}Fe_{1.83}O_3$ is similar to that of Sc (which is iso-valent with Fe) doped α-Fe_2O_3 (1 Sc atom per 30 atoms simulation cell) or Al-doped α-Fe_2O_3.[13, 46, 47] In the aforementioned structures, the spin up and spin down channels show slight shifts and local perturbations with respect to the pure α-Fe_2O_3, without introduction of new bands (of the dopant atom) within the original bandgap of pure α-Fe_2O_3. Similarly, for half-substituted Sc-hematite, the spin polarization is more significant and a crossing of the E-Fermi level in the spin down channel was observed.[14] Despite the polarization of the spin up and spin down channels in $Mg_{0.17}Fe_{1.83}O_3$, the bandgap remains indirect (Fig. 7b and 7c).

To further facilitate direct comparison with experiment, we computed the macroscopic dielectric tensor, which is directly related to the optical absorption spectrum. Inspection of Fig. 8 suggests that our computed macroscopic dielectric tensor is in good agreement with the experimental absorption spectra, which was obtained only in the accessible energy range. At higher frequencies the spectrum of $Mg_{0.17}Fe_{1.83}O_3$ is very similar to α-Fe_2O_3, and hence suggests that Mg-doping will not hamper the optical properties of α-Fe_2O_3 at the modeled concentration (Fig. 8a,b). However, at low energy, which was be-

yond the experimentally accessible range, the real part of the optical conductivity, and consequently the theoretically computed imaginary part of the dielectric function has a peak for $Mg_{0.17}Fe_{1.83}O_3$, known as a Drude peak, see Figure S9 in the SI.

(a)

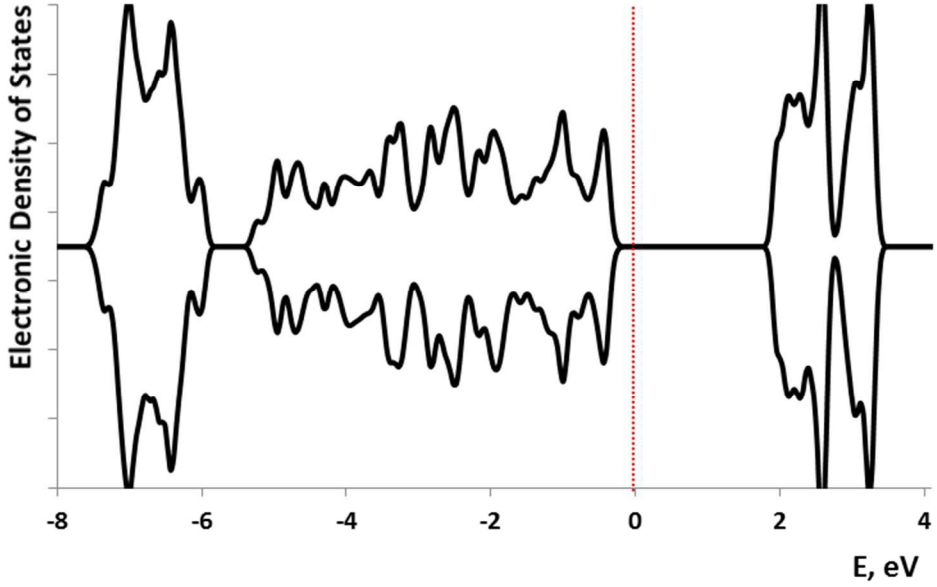

(b)

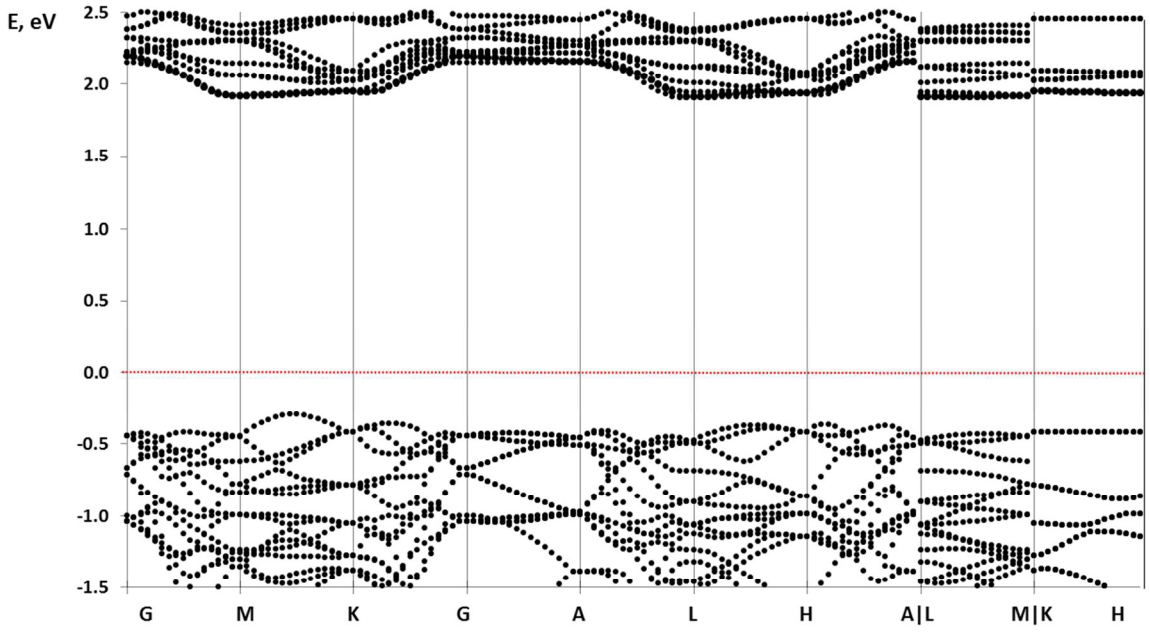

Figure 6. Electronic density of states (a) and band structure (b) of pure hematite, calculated at the PBE+U level of theory (U=4.3 eV). The Fermi energy is set to 0 eV and is indicated by a red dotted line.

(a)

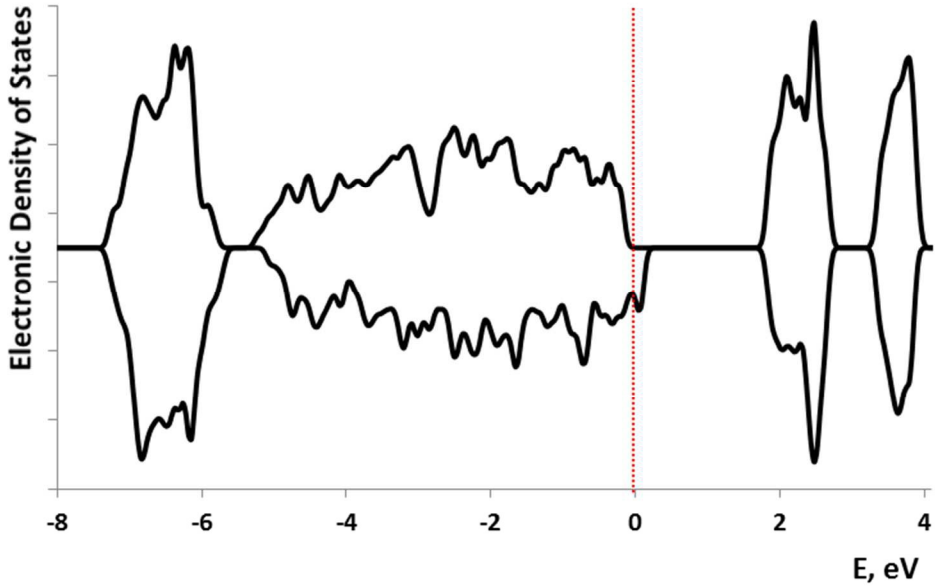

(b)

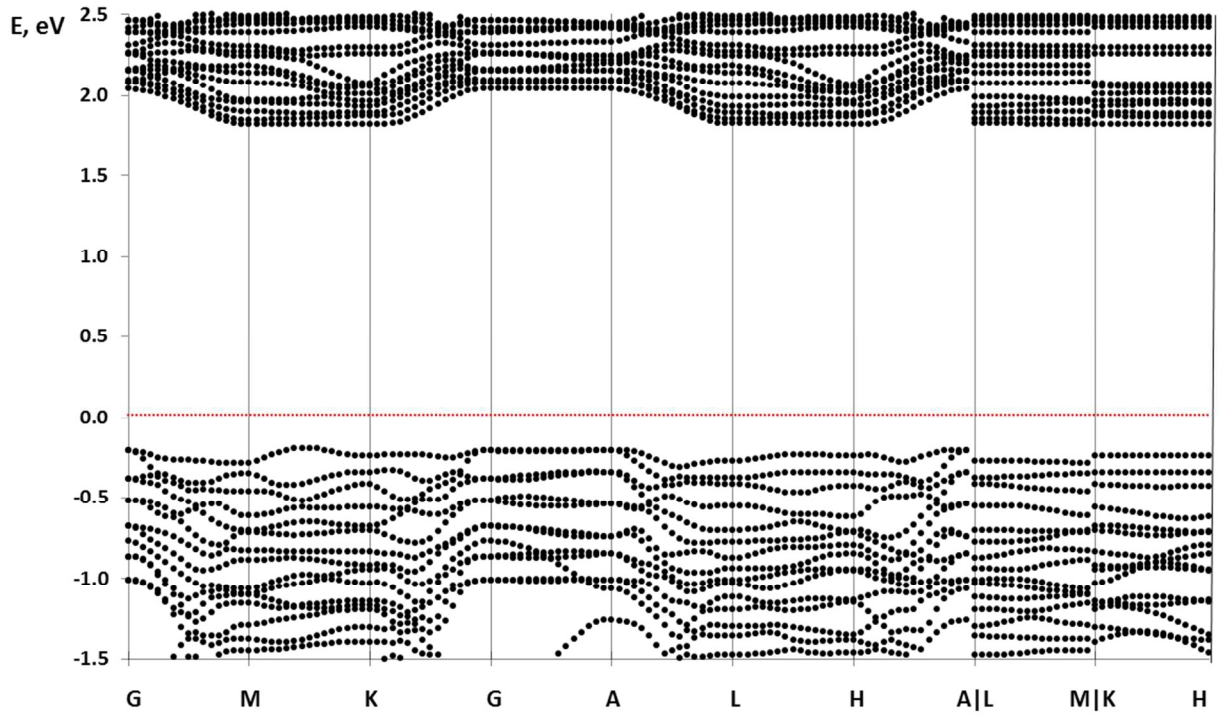

(c)

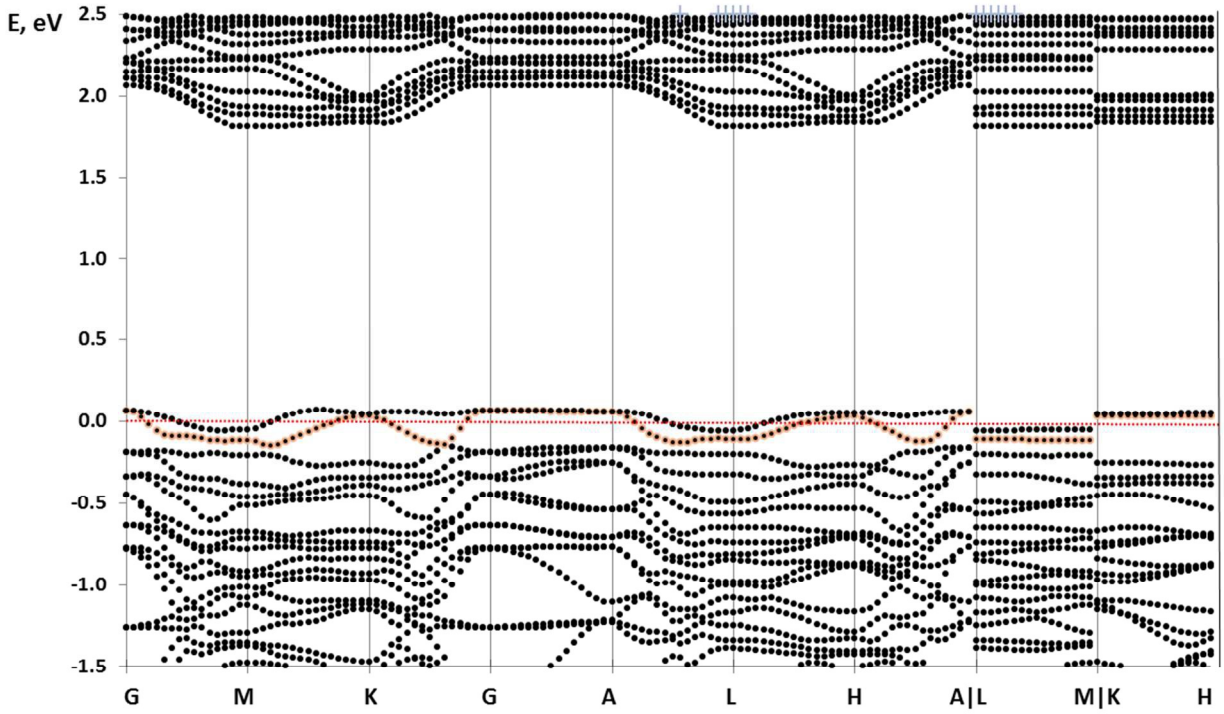

Figure 7. Electronic density of states (a) and band structure of (b) spin-up and (c) spin-down α-$Mg_{0.17}Fe_{1.83}O_3$, calculated at the PBE+U level of theory (U=4.3 eV). The Fermi energy is set to 0 eV and is indicated by a red dotted line.

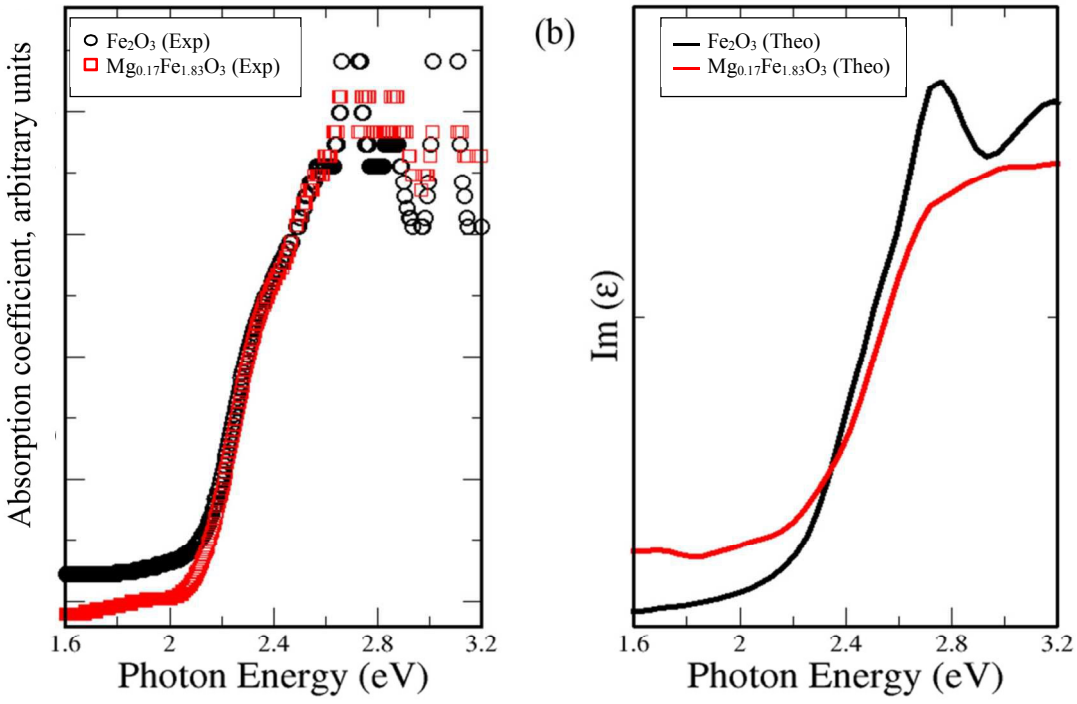

Figure 8. A comparison of (a) experimentally measured absorption coefficient and (b) our calculated imaginary part of the macroscopic dielectric constant for α-Fe_2O_3 (black) and $Mg_{0.17}Fe_{1.83}O_3$ (red) for the high energy range.

To summarize, the electronic structure analysis employing Bader electron partitioning, combined with the computed DOS, band-structure and optical properties, suggest that Mg induces only minor changes in the electronic structure of hematite. In particular, the Bader charge analysis is useful for understanding the changes in the electronic DOS of α-$Mg_xFe_{2-x}O_3$. We propose that the small impact of Mg-doping is due to the effective charge of Mg, which is very similar to that of Fe in α-$Mg_xFe_{2-x}O_3$. The computed charges suggest that Mg and Fe have very similar charges of ~+1.8 a.u., contrary to the formal oxidation state charges of +2 for Mg and +3 for Fe. We propose this as a reason Mg does not induce significant changes in hematite at the considered compositions of α-$Mg_xFe_{2-x}O_3$, x=0.04, 0.08, 0.17. To further test this assumption, we have performed a similar analysis for the hypothetical Ba analogue, i.e. α-$Ba_{0.17}Fe_{1.83}O_3$. The Bader partial charge of the Ba ion is reduced to 1.55 a.u. This results in charge polarization of its neighboring Fe and O atoms to 1.69 and -1.08, which is reflected in a pronounced change in the DOS of $Ba_{0.17}Fe_{1.83}O_3$ (Table S4 and Fig. S8), compared to pure α-Fe_2O_3 or α-$Mg_{0.17}Fe_{1.83}O_3$.

The bandgap calculations indicate that when the Mg/Fe ratio is 1/11 (i.e. 0.09) or lower, the bandgap changes in the spin-up and spin-down channels are small, similar to the experimental findings discussed in the previous section.

D. Evaluation of the nature of the chemical bond in α-Fe_2O_3 and α-$Mg_{0.17}Fe_{1.83}O_3$

To further dissect the effects at play in this material, we performed a chemical bond analysis using the off-site COHP and the energy integrated COHP (ICOHP) per bond for the nearest neighbors of Fe-O and Mg-O interactions for both spin channels (Fig. 9). The bonding and the antibonding contributions are indicated by a negative and a positive COHP, respectively. It is important to note that these COHP plots are associated with the Fe ion, which is in the spin-down sub-lattice of the unit cell. Hence, for the down spin channel, all the 3d-states of Fe^{3+} ion are completely filled and for the up spin channel, these states are above the Fermi level and remain empty (Fig.9a,b). This is consistent with the high spin state of the Fe^{3+} ($3d^5$) ions. In the up-spin channel of α-Fe_2O_3 (Fig. 9a), the COHP plot indicates strong covalency of the Fe-O pairs with the ICOHP value at the Fermi level of -0.72eV/bond. This situation changes dramatically for the up-spin channel of α-$Mg_{0.17}Fe_{1.83}O_3$ in which the ICOHP value at the Fermi level is only -

0.15 ev/bond (Fig. 9c). In the down spin channel, the ICOHP for the Fe-O pairs is 0.04 eV/bond in α-Fe_2O_3 and -0.15 eV/bond for Mg-O pairs in α-$Mg_{0.17}Fe_{1.83}O_3$ (Fig. 9b,d). Noticeably, the calculated partial DOS of α-Fe_2O_3 suggests that all the bonding states are primarily composed of O-2p states and the antibonding states are in close proximity to Fe-3d states for the up spin channel (refer top panel of COHPs, Fig. 9a). This is exactly opposite for the down spin channel where the bonding states are primarily composed of Fe-3d states and the antibonding states are O-2p states (refer top panel of COHPs, Fig. 9b). The COHP and ICOHP analysis indicate a weak covalent contribution in the Mg-O bond for both spin channels, and hence the ionic nature of Mg-O bond mentioned above. The results of the quantitative COHP scheme is in agreement with the charge density maps (Fig. 5a,b), which indicate a notable charge density in the Fe-O interatomic region (Fig. 5a), and no charge density in the Mg-O interatomic region (Fig. 5b), consistent with the ionic bonding of the latter.

The covalent and ionic characters of Fe-O and Mg-O bonds might have implications for their physical properties, such as stiffness of the material, which is manifested in its Bulk modulus. The computed bulk modulus of α-Fe_2O_3 is 202 GPa while that of α-$Mg_{0.17}Fe_{1.83}O_3$ is significantly lower at 193 GPa, indicating that α-$Mg_{0.17}Fe_{1.83}O_3$ is not quite as stiff as α-Fe_2O_3. This difference in Bulk moduli could be attributed to the Fe-O bond being more covalent, as discussed above, and hence stiffer. On the other hand, the Mg-O bonds are more ionic and hence the Mg-doped hematite is a softer material.

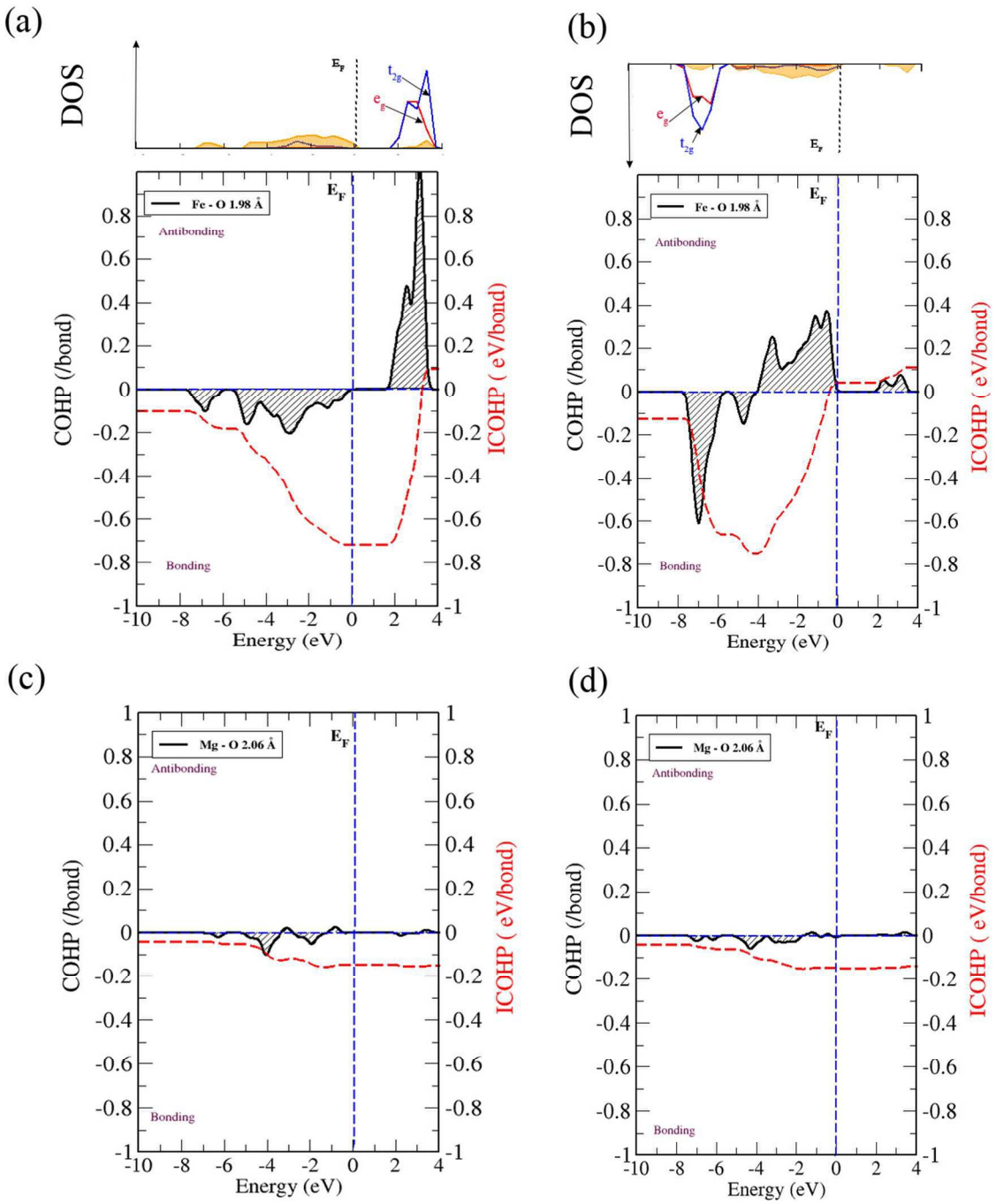

Figure 9. A comparison of off-site COHPs and ICOHPs (red) per bond for nearest neighbors of Fe - O in α-Fe_2O_3 spin up (a) and spin down (b) channels, and of Mg-O in $Mg_{0.17}Fe_{1.83}O_3$ spin up (c) and spin down (d) channels. All energies are relative to the Fermi energy. In addition, the corresponding density of states is shown for (a) and (b) on top of each COHP plots. For (c) and (d) there is no substantial DOS for the Mg ion near the Fermi level and thus the DOS is omitted.

Summary and Conclusions

Structural, optical and electronic properties of thin films of pure and Mg doped hematite were studied by means of atomistic DFT calculations and experimental measurements. The experimental absorbance bandgap analysis shows that up to Mg/Fe atomic ratios of 1/3 there is no significant change in the bandgap of $Mg_xFe_{2-x}O_3$. Assuming a hematite crystal structure and Mg substitution doping, the computed DFT+U eigenvalue bandgaps for x=0.17, 0.08 and 0.04 do not change significantly relative to pure hematite. Interestingly, Bader electron density partitioning analysis suggests that Mg and Fe have similar effective partial charges. This implies that introduction of holes upon Mg doping might not occur as in traditional semiconductors. This assumption is supported by experimental work by Tanget al.[20, 48] Based on these grounds we propose that in order to induce significant changes in the electronic structure of hematite, an ionic dopant of α-Fe_2O_3 should have a greater charge difference than that of Mg compared to Fe. Analysis of the nature of the chemical bond in these materials indicates that the Fe-O pair has a significant covalent contribution, while Mg-O is mostly ionic, and as a result Mg-doping of hematite results in a softening of the material.

Supporting Information. Additional information mentioned in the text, SF1-SF8, and ST1-ST4. This material is available free of charge via the Internet at _____

Corresponding Author

* majort@biu.ac.il

Author Contributions

†*These authors contributed equally to this work*

Acknowledgments

The authors acknowledge financial support from the Israeli National Nanotechnology Initiative (INNI, FTA project). MK acknowledges financial support from the Ministry of Absorption. HNB acknowledges financial support from the Ministry of Science, Technology and Space.

References

1. O. Neufeld and M. C. Toroker, *J. Phys. Chem. C*, 2015, **119**, 5836-5847.
2. T. Hisatomi, H. Dotan, M. Stefik, K. Sivula, A. Rothschild, M. Grätzel and N. Mathews, *Adv. Mater.*, 2012, **24**, 2699-2702.
3. K. Rajeshwar, P. Singh and J. DuBow, *Electrochim. Acta*, 1978, **23**, 1117-1144.
4. K. Sivula, F. Le Formal and M. Grätzel, *ChemSusChem*, 2011, **4**, 432-449.
5. S. Rühle, A. Y. Anderson, H.-N. Barad, B. Kupfer, Y. Bouhadana, E. Rosh-Hodesh and A. Zaban, *J. Phys. Chem. Lett.*, 2012, **3**, 3755-3764.
6. S. El-Molla, G. Fagal, N. Hassan and G. Mohamed, *Res Chem Intermed*, 2015, **41**, 679-689.
7. W. Tang, Y. Su, Q. Li, S. Gao and J. K. Shang, *Journal of Materials Chemistry A*, 2013, **1**, 830-836.
8. A. J. Bosman and H. J. Vandaal, *Adv. Phys.*, 1970, **19**, 1-&.
9. M. Huijben, G. Koster, M. K. Kruize, S. Wenderich, J. Verbeeck, S. Bals, E. Slooten, B. Shi, H. J. A. Molegraaf, J. E. Kleibeuker, S. van Aert, J. B. Goedkoop, A. Brinkman, D. H. A. Blank, M. S. Golden, G. van Tendeloo, H. Hilgenkamp and G. Rijnders, *Adv. Funct. Mater.*, 2013, **23**, 5240-5248.
10. Z. D. Pozun and G. Henkelman, *J. Chem. Phys.*, 2011, **134**.
11. Z. Deutsch, O. Schwartz, R. Tenne, R. Popovitz-Biro and D. Oron, *Nano Lett.*, 2012, **12**, 2948-2952.
12. G. Rollmann, A. Rohrbach, P. Entel and J. Hafner, *Phys. Rev. B*, 2004, **69**.
13. M. N. Huda, A. Walsh, Y. Yan, S.-H. Wei and M. M. Al-Jassim, *J. Appl. Phys.*, 2010, **107**, -.
14. H. Yang, W. B. Mi, H. L. Bai and Y. C. Cheng, *Rsc Advances*, 2012, **2**, 10708-10716.
15. C. Xia, Y. Jia, M. Tao and Q. Zhang, *Phys. Lett. A*, 2013, **377**, 1943-1947.
16. S. Kumari, A. P. Singh, Sonal, D. Deva, R. Shrivastav, S. Dass and V. R. Satsangi, *Int. J. Hydrogen Energy*, 2010, **35**, 3985-3990.
17. F. L. Souza, K. P. Lopes, P. A. P. Nascente and E. R. Leite, *Sol. Energy Mater. Sol. Cells*, 2009, **93**, 362-368.
18. L. Wang, C.-Y. Lee and P. Schmuki, *Electrochem. Commun.*, 2013, **30**, 21-25.
19. S. Mohanty and J. Ghose, *J. Phys. Chem. Solids*, 1992, **53**, 81-91.
20. H. W. Tang, M. A. Matin, H. L. Wang, M. Al-Jassim, J. Turner and Y. F. Yan, *J. Electron. Mater.*, 2012, **41**, 3100-3106.
21. A. Y. Anderson, Y. Bouhadana, H.-N. Barad, B. Kupfer, E. Rosh-Hodesh, H. Aviv, Y. Tischler, S. Rühle and A. Zaban, *ACS Comb. Sci.*, 2014, **16**, 53-65.
22. G. Kresse and J. Furthmuller, *Comput. Mater. Sci.*, 1996, **6**, 15-50.
23. G. Kresse and J. Furthmuller, *Phys. Rev. B*, 1996, **54**, 11169-11186.
24. G. Kresse and J. Hafner, *Phys. Rev. B*, 1993, **47**, 558-561.
25. G. Kresse and J. Hafner, *Phys. Rev. B*, 1994, **49**, 14251-14269.
26. P. E. Blochl, *Phys. Rev. B*, 1994, **50**, 17953-17979.
27. G. Kresse and D. Joubert, *Phys. Rev. B*, 1999, **59**, 1758-1775.
28. J. P. Perdew, K. Burke and M. Ernzerhof, *Phys. Rev. Lett.*, 1996, **77**, 3865-3868.
29. N. J. Mosey, P. Liao and E. A. Carter, *J. Chem. Phys.*, 2008, **129**.
30. S. L. Dudarev, G. A. Botton, S. Y. Savrasov, C. J. Humphreys and A. P. Sutton, *Phys. Rev. B*, 1998, **57**, 1505-1509.
31. G. Henkelman, A. Arnaldsson and H. Jonsson, *Journal of Chemical Physics*, 2006, **124**.
32. G. Henkelman, A. Arnaldsson and H. Jonsson, *Comput. Mater. Sci.*, 2006, **36**, 354-360.
33. E. Sanville, S. D. Kenny, R. Smith and G. Henkelman, *J. Comp. Chem.*, 2007, **28**, 899-908.
34. W. Tang, E. Sanville and G. Henkelman, *J. Phys.: Condens. Matter*, 2009, **21**.
35. S. Curtarolo, W. Setyawan, G. L. W. Hart, M. Jahnatek, R. V. Chepulskii, R. H. Taylor, S. Wang, J. Xue, K. Yang, O. Levy, M. J. Mehl, H. T. Stokes, D. O. Demchenko and D. Morgan, *Comput. Mater. Sci.*, 2012, **58**, 218-226.

36. M. Gajdoš, K. Hummer, G. Kresse, J. Furthmüller and F. Bechstedt, *Phys. Rev. B*, 2006, **73**, 045112-045120.
37. I. Aguilera, J. Vidal, P. Wahnón, L. Reining and S. Botti, *Phys. Rev. B*, 2011, **84**, 085145-085153.
38. P. Liao and E. A. Carter, *Phys. Chem. Chem. Phys.*, 2011, **13**, 15189-15199.
39. A. F. Lima, *J. Phys. Chem. Solids*, 2014, **75**, 148-152.
40. V. L. Deringer, A. L. Tchougréeff and R. Dronskowski, *J. Phys. Chem. A*, 2011, **115**, 5461-5466.
41. R. Dronskowski and P. E. Bloechl, *J. Phys. Chem.*, 1993, **97**, 8617-8624.
42. S. Maintz, V. L. Deringer, A. L. Tchougréeff and R. Dronskowski, *J. Comp. Chem.*, 2013, **34**, 2557-2567.
43. S. Jana, V. Singh, A. Nag, C. Meneghini, I. Dasgupta, G. Aquilanti and S. Ray, *Phys. Rev. B*, 2012, **86**, 014203.
44. N. F. Chayed, N. Badar, R. Rusdi, N. Kamarudin and N. Kamarulzaman, in *International Congress on Advances in Applied Physics and Materials Science*, eds. M. H. Aslan, A. Y. Oral, M. Ozer and S. H. Caglar, 2011, vol. 1400, pp. 328-332.
45. R. L. Blake, Hessevic.Re, T. Zoltai and L. W. Finger, *Am. Mineral.*, 1966, **51**, 123-&.
46. A. Kleiman-Shwarsctein, M. N. Huda, A. Walsh, Y. Yan, G. D. Stucky, Y.-S. Hu, M. M. Al-Jassim and E. W. McFarland, *Chem. Mater.*, 2010, **22**, 510-517.
47. R. Rivera, H. P. Pinto, A. Stashans and L. Piedra, *Phys. Scr.*, 2012, **85**.
48. Y. W. Tai, C. C. Yang, M. H. Yang, C. S. Hong, H. H. Lin and B. Z. Wan, *Journal of the Taiwan Institute of Chemical Engineers*, 2011, **42**, 669-673.